Magnetic Resonance Imaging 100 (2023) 84–92

Contents lists available at ScienceDirect

Magnetic Resonance Imaging

journal homepage: www.elsevier.com/locate/mri

In vivo detection of penetrating arteriole alterations in cerebral white matter in patients with diabetes with 7 T MRI

Xiaopeng Zong [a,b,*,1], Jordan Jimenez [a], Tengfei Li [a,b], William J. Powers [c]

[a] Biomedical Research Imaging Center, Durham, NC 27599, USA
[b] Department of Radiology, University of North Carolina at Chapel Hill, Durham, NC 27599, USA
[c] Department of Neurology, Duke University School of Medicine, Durham, NC 27599, USA

ARTICLE INFO

Keywords:
Cerebral small vessel disease
Cerebral arterioles
White matter
Small vessels
Brain blood vessels
Phase contrast MRI
Diabetes mellitus

ABSTRACT

Cerebral small vessel disease (SVD) is responsible for primary intracerebral hemorrhages, lacunar infarcts and white matter hyperintensity in T_2 weighted images. While the brain lesions attributed to small vessel disease can be characterized by conventional MRI, it remains challenging to noninvasively measure the early pathological changes of the small underlying vessels. We evaluated the feasibility of detecting alterations in white matter penetrating arterioles (PA) in patients with diabetes with ultra-high field 7 T MRI.

19 participants with diabetes mellitus (DM) and 19 age- and sex-matched healthy controls were scanned with whole brain T_2 and susceptibility weighted MRI and a single slice phase contrast MRI 15 mm above the corpus callosum. The PC-MRI scans were repeated three times. PA masks were manually drawn on the first images after anonymization or automatically segmented on all three images. For each PA, lumen diameter, flow velocity and volume flow rate were derived by model-based analyses of complex difference images. Quasi-Poisson regression was performed for PA count using disease condition, age, and sex as independent variables. Linear mixed effect model analyses were performed for the other measurements using disease condition and age as fixed effect and participant pair specific disease condition as random effect.

No severe radiological features of SVD were observed in T_2 and susceptibility weighted images in any of the participants except for white matter hyperintensities with Fazekas score of 1 or 2 in 68% and 26% of patients and controls, respectively. The minimum diameter of visible PA was 78 μm and the majority had diameters <250 μm. Among the manually segmented PA with tilt angle less than 30° from the slice normal direction, flow velocities were lower in the DM group (1.9 ± 0.6 vs. 2.2 ± 0.6; $p = 0.022$), while no significant difference was observed in count, diameter, or volume flow rate. Similar results were observed in the automatically segmented PA. We also observed significantly increased diameter or decreased velocity with age in some of the scans. This study suggests that early PA alterations that are discriminative of disease state and age might be detectable in human cerebral white matter with 7 T MRI in vivo.

1. Introduction

Cerebral small vessel diseases (SVD) are a group of neuropathological processes caused by dysfunctions of small blood vessels in the brain. Three pathological subforms of subcortical small vessel disease are distinguished: arteriosclerosis/microatheroma in 200–800 μm diameter arterioles, fibrinoid necrosis/lipohyalinosis of 40–300 μm diameter arterioles and concentric hyaline thickening/ateriolosclerosis of 40–150 μm diameter arterioles [1]. These three often occur in the same brains and often, but not invariably, in the setting of longstanding arterial hypertension or diabetes [2,3]. Disease of these vessels is responsible for primary intracerebral hemorrhages and discrete small cerebral infarcts

Abbreviations: SVD, small vessel diseases; PA, penetrating artery; PVS, peri-vascular space; PA_{perp}, PA that could be matched to PVSs and approximately perpendicular to imaging slice.; WM, white matter; DM, diabetes mellitus; HC, health controls; FatNav, fat navigator; TSE, turbo spin echo; PC, phase contrast; SWI, susceptibility weighted imaging; WMH, what matter hyperintensities; MBAC, model based analyses of complex difference image; D_{PA}, lumen diameter; V_{PA}, flow velocity; Q_{PA}, volume flow rate.

* Corresponding author at: Biomedical Research Imaging Center, Durham, NC 27599, USA.
E-mail address: zongxp@shanghaitech.edu.cn (X. Zong).
[1] Present address: School of Biomedical Engineering, ShanghaiTech University, 393 Middle Huaxia Road, Pudong New District, Shanghai, China

https://doi.org/10.1016/j.mri.2023.03.015
Received 13 January 2023; Received in revised form 16 March 2023; Accepted 21 March 2023
Available online 24 March 2023

(lacunar infarcts) in the deep gray nuclei and white matter (WM) [1]. Together these make up one-third of all strokes [2,4]. In addition, SVD causes the more diffuse widespread WM hyperintensities (WHM) in T_2 weighted images, which are characterized by demyelination, axonal loss and gliosis without frank infarction [1]. Earlier studies found WM lesions in 56% and 96% of participants with no history of stroke and with ages ≥40 years [5] and ≥ 65 years [6], respectively. Silent brain infracts were found in 14.2% and 21% of subjects with ages ≥40 years [5] and ≥ 60 years [7], respectively. More severe SVD is associated with increased cognitive [6,8], psychiatric [9], and physical disabilities [6,10,11].

The prevalence, distribution and degree of SVD is inferred from the prevalence and degree of the end organ damage manifested by intracerebral hemorrhage, lacunar infarcts and WMH [12]. While these brain lesions attributed to SVD can be characterized due to their larger sizes and clear visualization by conventional MRI, it remains challenging to noninvasively measure the early pathological changes of the underlying small vessels. Post-mortem data demonstrate that the penetrating arteries (PAs) in WM are important foci for SVD [13,14]. An imaging method for measuring the early structural and functional changes of PAs in WM in vivo for both cross-sectional and longitudinal studies would help to illuminate the etiopathogenesis of SVD and help develop effective treatment strategies.

Structural changes can be inferred by measuring the size of PAs, while functional changes can be inferred by measuring their flow velocity and pulsatility. In this study, we evaluated the feasibility of detecting differences in the size and flow characteristics of WM PAs between patients with diabetes mellitus (DM) and healthy controls (HC) with ultra-high field 7 T MRI. PA diameter and flow velocity can be obtained after correcting for partial volume effects by model based analyses of complex difference images (MBAC) [15]. Although age [16,17], blood pressure [18], and SVD [19] related pulsatility alterations have been reported, pulsatility measurement was not pursued here as we only focused on quantitative measures of PAs, which requires sufficient signal to noise ratio (SNR) at individual PA level to perform MBAC from phase contrast (PC) MRI for correcting partial volume effects [15]. Separation of the data into multiple cardiac phases will make the SNR insufficient.

2. Material and methods

2.1. Study design

This initial study was designed to determine the feasibility of further studies using PC-MRI and MBAC. The study was designed as a cohort study comparing participants with DM to age- and sex-matched HC.

2.2. Subject and recruitment procedure

This study was approved by the Institutional Review Board of the University of North Carolina at Chapel Hill. Informed consent was obtained from each subject. Patients registered in the North Carolina Data Warehouse for Health who met the following criteria were invited by email to participate in the study: ages 30–70 yrs.; history of DM for 10 years or longer, and no history of brain disease or abnormalities on a prior brain MRI scan if available. HC were recruited from the general population by mass emails using the following criteria: no history of diabetes, hypertension, or brain disease, and absolute age difference between DM and matched control ≤3 years. Exclusion criteria for both groups were pregnancy, breastfeeding, and unable or unsafe to complete the MRI scan.

22 patients and 20 HC were recruited. Images were evaluated by a neurologist and a radiologist for possible abnormalities. One partient had a ~ 2 cm cavernous malformation in deep WM and another had severe motion artifacts. Furthermore, one subject came out of the scanner during the scan which disabled the registration of fat navigator (FatNav) images between scans which was used to correct head motion between scans. This participant and his/her matched control were excluded, resulting in 19 participants in each group.

2.3. Cognitive and clinical data

The Mini MoCA version 2.1 was administered to each particpant to evaluate different cognitive domains, including attention, concentration, executive functions, memory, language, and orientation. The total score is 15 and a final total score of 11 or above is considered normal [20].

Blood glucose level was measured using a Care Touch Diabetes Testing Kit (Brooklyn, NY, USA) prior to the MRI scan in each subject. Additional clinical data including medical history and cardiovascular risk factors were collected through a questionnaire or retrieved from medical records when available. Lipid panels, including HDL, LDL, total cholesterol, non-HDL cholesterol, and triglyceride, and A1C levels are reported only if they were measured within 180 days prior to the MRI scan.

2.4. MRI protocol

All images were acquired using a Nova 32-channel receive and single-channel volume transmit coil on a 7 T MRI scanner (Siemens Healthineer, Erlangen, Germany). High resolution whole-brain turbo spin echo (TSE) and double-echo susceptibility weighted imaging (SWI), and single slice PC-MRI covering the centrum semiovale were acquired. The PC-MRI scan had a VENC of 4 cm/s with one-sided encoding and was repeated three times. No k-space undersampling was used to avoid g-factor penalty on SNR. No cardiac gating was used, as pulsatility was not measured and more repetitions would be required to acquire full k-space data at all cardiac phases which would prolong scan time. A high flip angle of 45° was used to enhance the blood signal in PAs and suppress the WM signal [21], since the blood water protons would not be saturated to the steady-state value before leaving the slice due to flow. The VENC of 4 cm/s was chosen as the mean velocity for the majority of PAs was ~2 cm/s. As the flow velocity is higher at the center of the vessels, lower VENC might cause phase wrapping at vessel center. The slice was positioned 15 mm above the corpus callosum and parallel to the anterior commissure – posterior commissure line. Prospective motion correction was performed during the TSE and PC-MRI scans based on fat navigator (FatNav) images acquired throughout the scans [22]. As the slice was prescribed based on the TSE images, to correct for potential motion between the TSE and PC MRI scans, the FatNav images in PC MRI were registered to the first FatNav image from the TSE-MRI scan. To aid the quantitative analysis of PC-MRI images and WM property, T_1 and T_2* maps were also acquired at the same slice position as the PC-MRI using variable TR TSE and multi-echo gradient echo sequences, respectively. The sequence parameters of all sequences can be found in Table 1. Representative whole brain TSE and SWI images can be found in Supplementary Material Fig. 1S.

2.5. T_1 and T_2* maps

T_1 was obtained at each voxel by nonlinear fit of the signal recovery function to the image intensity versus TR curve from the T_1 mapping scan. T_2* was obtained at each voxel by nonlinear fit of the exponential signal decay function to the image intensities versus TE curve. T_1 and T_2* values were calculated as the averages over two small ovals (total area ~ 1.6 cm^2) manually drawn within the normal appearing WM in the two hemispheres.

2.6. Head motion parameters

Head motion can have detrimental effects on image quality and can introduce artificial differences in small vessel parameters between the patients and controls. To compare the motion severities between the two

Table 1
MRI parameters for the TSE, SWI, PC, FatNav, T_1 and T_2* mapping sequences. In the PC sequence, VENC = 4 cm/s and a one-sided flow encoding gradient was employed, whereby the flow encoding gradient was turned on and off alternatingly.

	TSE	SWI	PC	FatNav	TSE (T1 map)	GRE (T2* map)
TE (ms)	326	7.59/15	15.7	1.31	8.5	5.6–53 (10 values)
TR (ms)	3300	21	30	3 (TSE) 30 (PC)	200 to 8000 (10 values)	60
FOV (mm^3)	210 × 210 × 99.2	220 × 179	200 × 162.5 × 2	222 × 198 × 210	200 × 162.4	200 × 162.5
Acquired voxel size (mm^3)	0.41 × 0.4 × 0.4	0.49 × 0.49 × 0.5	0.31 × 0.52 × 2	3 × 3 × 3	1.56 × 1.56 × 2	0.625 × 0.625 × 2
Recon voxel Size (mm^3)	0.41 × 0.41 × 0.4	0.49 × 0.49 × 0.5	0.156 × 0.156 × 2	3 × 3 × 3	1.562 × 1.562 × 2	0.625 × 0.625 × 2
Recon matrix Size	512 × 512 × 248	364 × 448 × 192	1280 × 768	74 × 66 × 70	128 × 104	320 × 260
FA (degree)	Variable	10	45	7 (TSE) 14 (PC)	90°, 180°	13°
Slice Orientation	Axial	Axial	Oblique axial	Axial	Oblique axial	Oblique axial
Partial Fourier Factor	0.79 × 0.625	0.75 × 0.75	1	0.75 × 0.75	1	0.875
GRAPPA factor	3 × 1	3 × 1	1	4 × 4	3	2
GRAPPA ACS lines	24	30	NA	21 × 23	32	24
Bandwidth (Hz/Pixel)	349	150	73	1931 (TSE) 1959 (PC)	260	290
TA	8:03 min	5:06 min	3:13 min (10 repeats)	4.68 s (PC) 0.47 s (TSE)	3:54 min	1:16 min

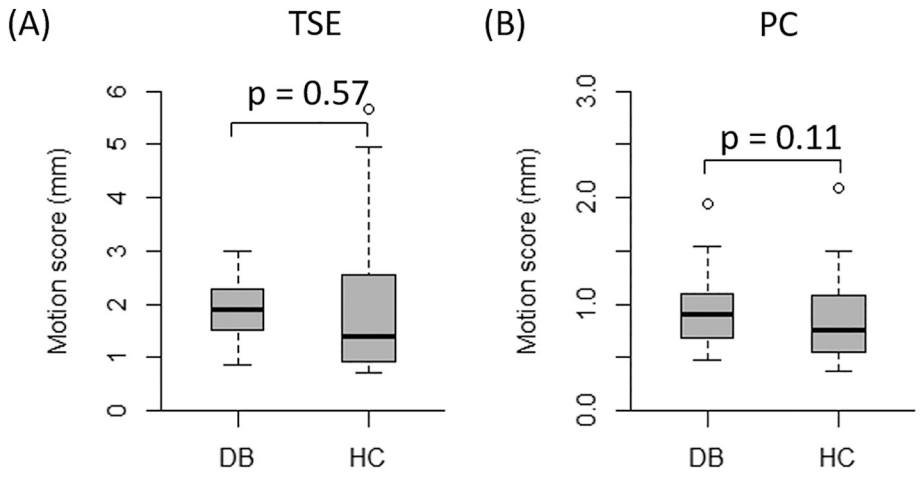

Fig. 1. Boxplots of motion scores in (A) TSE and (B) PC MRI scans. The motion scores from the three PC-MRI scans were averaged in (B). The *p* values from signed rank tests are also given.

groups, we calculated motion scores based on the FatNav images which were defined as the sum of rotational and translational motion ranges in each scan [22]. In addition, to characterize the degree of sudden and fast motions, we performed a 5th order polynomial fit to the motion parameter time courses to remove the slow motion from the time courses and calculated the root mean square of the fit residual.

2.7. PA parameters

PA masks were manually drawn by one of the authors (XZ) on the first PC-MRI image of each subject, after anonymizing the images. PAs were defined as hyperintensive clusters in the phase images inside WM. To control for false positive voxels, each hyperintensive cluster had to overlap with a hyperintensive cluster on the corresponding magnitude image with flow encoding gradient off. PAs from all scans were also segmented using a recently developed automatic segmentation algorithm based on convolutional neural networks [22].

From the segmented PA clusters, those that could be matched to perivascular spaces (PVSs) imaged by the whole brain TSE sequence and had a tilt angle ≤30 degrees from the slice normal direction (named PA_{perp} below) were selected and analyzed by MBAC [15] to derive lumen diameter (D_{PA}), flow velocity (V_{PA}) and volume flow rate (Q_{PA}). The model parameters were the same as those previously published except for T_1 and T_2* in WM which were set to the measured mean T_1 (=1.3 s) and T_2* (=27.7 ms) values [15]. To obtain the angle between a PA and the slice normal direction in PC-MRI, PVS masks automatically segmented using the M2EDN algorithm [23] were resampled at the same slice position as the PC-MRI scan. Then their positions were manually shifted in-plane so that maximum numbers of PVSs were visually matched to PAs. After such manual adjustment, matched PA-PVS pairs were defined as those whose centers were within 1 mm (6 voxels) of each other. However, if a PA (PVS) could be matched to more than one PVSs (PA), it was excluded. The PA orientations were assumed to be the same as those of the matched PVSs and the details for determining PVS orientations have been described before [15]. An example of PC-MRI and resampled TSE images, as well as matched and unmatched PA and PVS masks, can be found in the Supplementary Material Fig. 2S.

To evaluate the reproducibility, the count, D_{PA}, V_{PA}, and Q_{PA} of PAs from the first and third scans were used to generate Bland-Altman plots and calculate coefficients of repeatability. Two different counts were calculated, one for all segmented PAs and the other for PA_{perp}. For D_{PA}, V_{PA}, and Q_{PA}, the Bland-Altman plots were generated using individual PA_{perp} that could be matched between scans 1 and 3, using the same matching procedure as described above except for allowing a maximum separation of 2 mm.

2.8. Statistical analysis

The primary analyses were between-group differences for each of the four PA measurements (PA count (N_{PA}), D_{PA}, V_{PA}, and Q_{PA}) in the

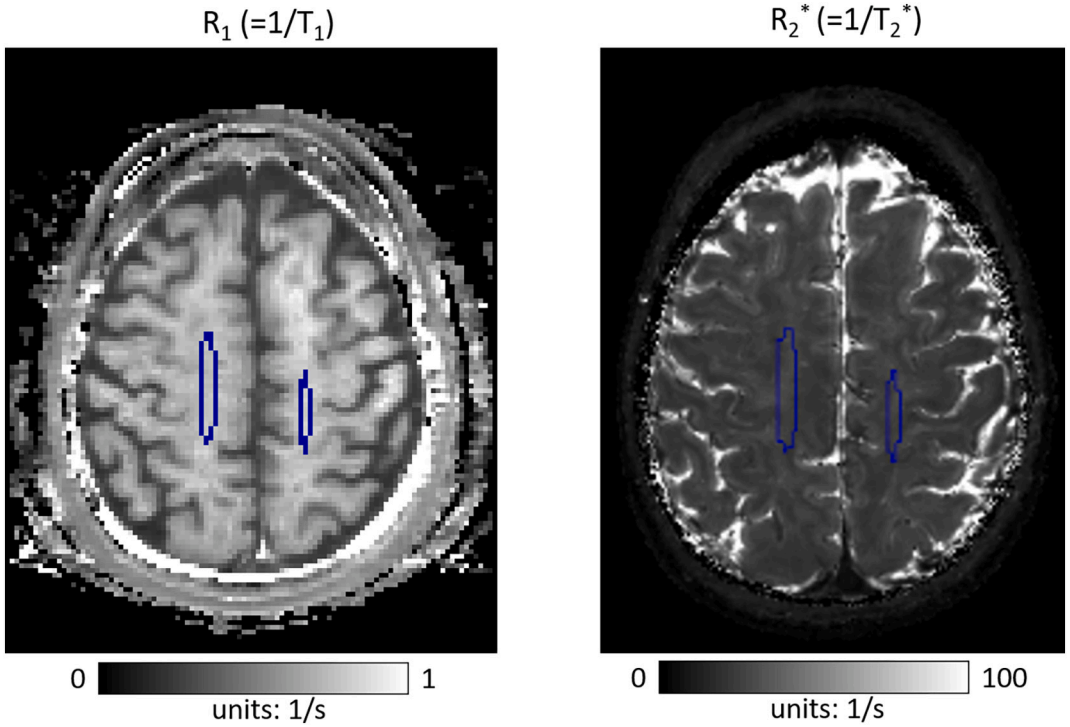

Fig. 2. Example R_1 and R_2* maps and manually drawn white matter ROIs used for calculating the mean R_1 and R_2* values.

segmented PAs. Quasi-Poisson regression was performed for PA counts using disease condition (binary as yes/no), age, and sex as independent variables because the residual deviance from Poisson regression showed significant overdispersion (dispersion test, $p < 0.024$).

A linear mixed effects model was used for the regression analysis of the other measurements, which incorporated both fixed and random effects. The fixed effect was the disease condition, and the random effect was specific to each participant pair and related to the disease condition. This approach allows for the modeling of both population-level and individual-level differences in the relationship between the disease condition and the outcome being analyzed. The same analyses were performed for automatically segmented PAs from each of the three scans to test robustness of the manual segmented PA results. One subject had wrong slice placement and another had no PAperp from the second PC-MRI scan, resulting in 18 and 17 pairs for the second scan in the regression analyses of counts and the other PA parameters, respectively. In order to study age effects on D_{PA}, V_{PA}, and Q_{PA}, a second linear mixed effects model was analyzed by additionally including age as the second fixed effect.

Since this was an initial feasibility study of a new technique with a relatively small number of subjects, we set a priori a futility boundary such that if any one of the four comparisons in the primary analyses produced an $\alpha < 0.05$, we would declare non-futility. Failure to reject the null hypothesis of one or more of these four comparisons at this level is equivalent to a false discovery rate of no more than 0.20. Clinical data are provided for informative purposes without statistical tests performed.

3. Results

Table 2 provides a summary of the clinical data. DM participants had higher weight, body mass index, systolic blood pressure, blood glucose level, and more with hypertension and a history of smoking. MoCA cognitive scores, lipid panel results, and diastolic blood pressure were comparable between groups. No microbleeds were found in any participant and only one DM participant had a 5 mm lacunar infarct in the caudate nucleus. More DM participants had white matter hyperintensities (total Fazekas scores >0 [24]), as graded by a neurologist (coauthor WJP) on the whole brain TSE images.

Table 2
Summary of demographic and clinical data. The numbers in parentheses that are connected by dashes are the total range, while the numbers after "n=" are the total subjects for whom the data is available.

	Patient (n = 19)	Control (n = 19)
Diabetes type	1 (n = 9), 2 (n = 10)	N/A
Age (yr)	57.2 (37.0–69.0)	56.7 (34.0–70.0)
Weight (kg)	84.8 (49.9–105.2)	74.5 (46.3–99.8)
Height (cm)	171.9 (154.9–185.9)	173.8 (157.5–185.4)
BMI (kg/m2)	28.6 (20.8–33.5)	24.6 (18.7–37.4)
Systolic BP (mmHg)	130.5 (115.0–164.0)	120.7 (105.0–148.0)
Diastolic BP (mmHg)	75.1 (53.0–89.0)	73.1 (56.0–90.0)
Blood glucose level (mg/dL)	178.3 (107.0–333.0)	112.9 (88.0–180.0)
A1C (%)	7.2 (5.5–14.0)	6.5 (6.5–6.5)
Cholesterol/HDL	3.6 (2.0–6.8)	3.2 (2.2–5.3)
Cholesterol (mg/dL)	204.0 (199.0–211.0)	184.5 (112.0–216.0)
HDL (mg/dL)	77.0 (31.0–103.0)	61.5 (40.0–85.0)
LDL (mg/dL)	104.7 (86.0–137.0)	91.0 (15.0–154.0)
Non HDL Cholesterol (mg/dL)	127.0 (99.0–180.0)	123.0 (62.0–171.0)
Triglyceride (mg/dL)	110.3 (54.0–213.0)	78.5 (60.0–111.0)
History of smoking	13	2
MoCA	12.7 (10.0–15.0)	13.3 (12.0–15.0)
WMH Fazekas score	2 (n = 4), 1 (n = 9), 0 (n = 6)	2 (n = 2), 1 (n = 3), 0 (n = 14)
Lacunar infarct	Yes (n = 0), no (n = 19)	yes (n = 0), no (n = 19)

The motion scores were comparable between DM participants and controls in both the TSE ($p = 0.57$; Wilcoxon's signed rank test) and PC-MRI ($p = 0.11$; Wilcoxon's signed rank test) scans, as shown in Fig. 1. The motion ranges were 0.36–2.3 mm and 0.10–2.3 mm in the DM and HC groups, respectively, in the PC-MRI scans. 53% and 35% of scans had motion scores >0.8 mm in the two groups, respectively. The residuals for each of the motion parameters in PC-MRI scans after 5th polynomial fit are provided in Table 3, as well as the p values from signed rank tests comparing the difference between the groups. The DM group had

Table 3
The root mean square of the residuals of motion parameters after 5th polynomial fit to their time courses. The last row shows p-values from Wilcoxon's signed rank tests.

	Rotation (deg)			Translation (mm)		
	Roll	Pitch	Yaw	IS	RL	AP
DB	0.021 (0.010)	0.036 (0.026)	0.026 (0.014)	0.044 (0.024)	0.039 (0.016)	0.022 (0.008)
HC	0.018 (0.011)	0.033 (0.017)	0.024 (0.016)	0.036 (0.031)	0.024 (0.015)	0.024 (0.011)
p value	0.033	0.98	0.44	0.05	5.2e-05	0.32

significantly higher residual in translation along RL direction, suggesting increased severity of fast motion.

The R_1 ($1/T_1$) and R_2* ($1/T_2$*) values were not significantly different between the patients and controls ($p = 0.81$ and 0.12, respectively; Wilconxon's signed rank test). Averages over all subjects were (mean ±std) $R_1 = 0.76 \pm 0.03\ s^{-1}$ and $R_2* = 36.1 \pm 3.5\ s^{-1}$. Representative R_1 and R_2* maps and manually drawn ROIs can be found in Fig. 2.

Fig. 3 provides representative magnitude (with velocity encoding (VENC) gradient off) and phase difference (between VENC on and off) images and segmented PA clusters. In 97% cases, the manual segmentation identified more PA clusters than automatic segmentation. Using the manual segmentation as the ground truth, the positive predictive value, sensitivity, and dice similarity index (mean ± std) for identifying PA clusters were 0.94 ± 0.05, 0.73 ± 0.09, and 0.81 ± 0.06, respectively.

More PAs were segmented in the HC than in DM group in all three scans, although the differences were not statistically significant ($p \geq 0.13$, quansi-Poisson regression). Only a small fraction (~19%) of the segmented PAs are PA_{perp}, i.e., can be matched to PVSs and had tilt angle $\leq 30^o$. The PA_{perp} count was not significantly different between the groups ($p \geq 0.76$, quasi-Poisson regression). The mean total and PA_{perp} counts and the p values for quasi-Poisson regressions can be found in the first 8 rows of Table 4. There was no significant age effects in the total PA or PA_{perp} counts, although a tendacy towarding decreasing count with aging is observed in all scans, as shown in the first 8 rows in Table 5.

Figs. 4 – 6 show the historgrams of the D_{PA}, V_{PA}, and Q_{PA} calculated from MBAC for the manually segmented PA_{perp}, respectively. The minimum D_{PA} was 78 μm and most D_{PA} were <250 μm. V_{PA} was lower in the DM than HC group (1.9 ± 0.63 vs. 2.2 ± 0.63 cm/s, $p = 0.02$) meeting the pre-specified criterion of $p < 0.05$. Significant difference was also observed between groups in velocity calculated from the automatically segmented PA_{perp} in the second scan, while non-signficantly lower velocity in the DM group was also observed in the other two scans. The mean D_{PA}, V_{PA}, and Q_{PA} and the p values for linear mixed effect regressions can be found in the last 12 rows of Table 4. The Bland-Altman plots of the total PA count, the PA_{perp} count, D_{PA}, V_{PA}, and Q_{PA} are shown in Fig. 7, with coefficients of repeatability 12.2, 3.1, 0.09 mm, 0.76 cm/s, and 0.19 mm^3/s, respectively.

None of the p-values for between group differences of D_{PA} and Q_{PA} were < 0.05. D_{PA} significantly increased with age in scan 3, while the opposite trend was observed in V_{PA} in scan 1. Consistent trend was observed among most scans, although they did not reach statistical significance. The significance of disease effects remained the same as above after adding age as the additional factor in the model. The age coefficients for D_{PA}, V_{PA}, and Q_{PA} can be found in the last 12 rows in Table 5.

As the tilt angle differences of PAs between groups can affect the MBAC results [15], we compared the distribution of PA tilt angles for PA_{perp} in Fig. 8. There was no significant difference in tilt angles between the DM and HC groups for either the manually or automatically segmented masks ($p = 0.76$ or 0.80; linear mixed effect model).

4. Discussion

Our study suggests PA properties that might be discriminative of disease state can be quantitatively measured in human cerebral WM with 7 T MRI in vivo. The PA flow velocity was consistently lower in DM participants in all three scans while tissue properties as reflected in R_1

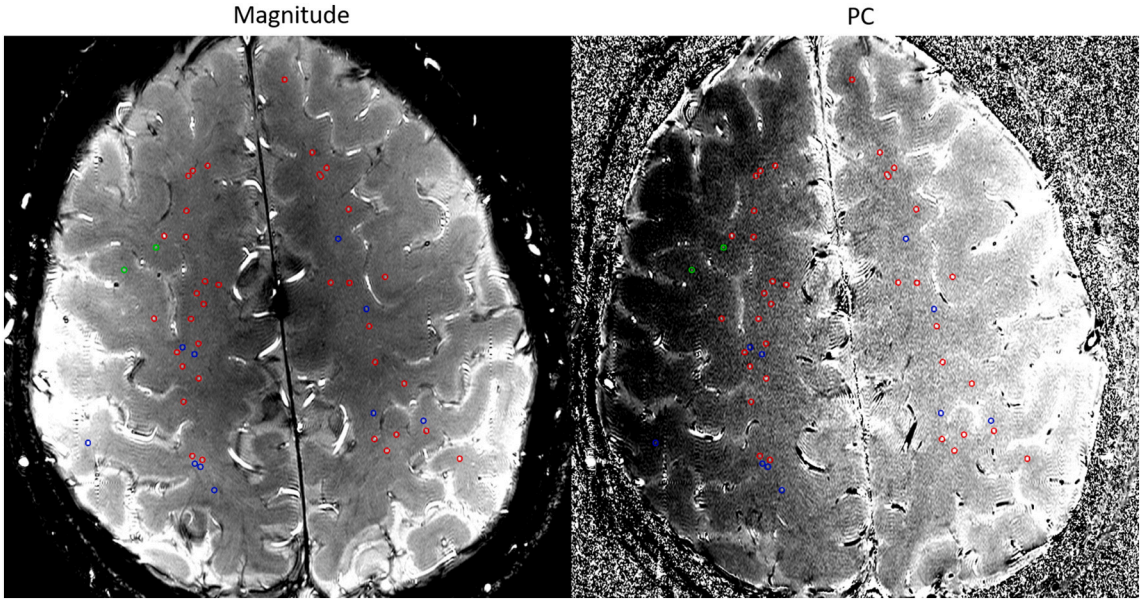

Fig. 3. Magnitude (with velocity encoding gradients off) and phase difference (between VENC on and off) images in a representative subject. The red, green, and blue circles surround penetrating arteries that were segmented in both manual and automatic methods, only in the automatic method, and only in the manual method, respectively. (For interpretation of the references to colour in this figure legend, the reader is referred to the web version of this article.)

Table 4
Summary of mean penetrating artery (PA) count, mean count of PAs that can match a perivascular spaces (PVS) and has angles $\leq 30^{o}$ from the slice normal direction, diameter (D_{PA}), flow velocity (V_{PA}), and volume flow rate (Q_{PA}) in patients (column 2) and healthy controls (column 3). Columns 4 and 5 list the differences between patients and controls and *p* values (number of pairs), respectively, which were estimated from the quasi-Poisson regression (for count) and linear mixed effects model analyses. In column 4, the differences for counts represent normalized differences. Only vessels that had tilt angles $\leq 30^{o}$ were included in calculating D_{PA}, V_{PA}, and Q_{PA}. Significant difference is indicated by an asterisk in the last column.

	Segmentation	Scan	Patient	Healthy controls	Difference	P value (n)
PA Count	Manual	1	35 (16)	42 (17)	0.21 (0.15)	0.17 (19)
	Auto	1	28 (14)	31 (13)	0.1 (0.15)	0.5 (19)
	Auto	2	28 (13)	34 (16)	0.19 (0.16)	0.24 (18)
	Auto	3	29 (14)	37 (16)	0.24 (0.15)	0.13 (19)
PA_{perp} Count	Manual	1	6.8 (4.5)	6.8 (5)	0.0082 (0.23)	0.97 (19)
	Auto	1	5.3 (3.8)	5.4 (3.9)	0.03 (0.24)	0.89 (19)
	Auto	2	5.0 (2.8)	5.6 (4.6)	0.12 (0.23)	0.57 (18)
	Auto	3	5.6 (3.5)	6 (4.9)	0.064 (0.23)	0.76 (19)
D_{PA} (mm)	Manual	1	0.15 (0.06)	0.14 (0.05)	0.003 (0.01)	0.79 (19)
	Auto	1	0.16 (0.06)	0.15 (0.06)	–0.008 (0.02)	0.67 (19)
	Auto	2	0.17 (0.07)	0.15 (0.06)	0.018 (0.013)	0.18 (17)
	Auto	3	0.16 (0.06)	0.15 (0.043)	0.011 (0.011)	0.34 (19)
V_{PA} (cm/s)	Manual	1	1.9 (0.6)	2.2 (0.6)	–0.27 (0.11)	0.022 (19)*
	Auto	1	1.9 (0.6)	2.1 (0.6)	–0.2 (0.12)	0.11 (19)
	Auto	2	1.7 (0.6)	2.0 (0.6)	–0.31 (0.13)	0.025 (17)*
	Auto	3	1.8 (0.6)	2.0 (0.6)	–0.22 (0.13)	0.12 (19)
Q_{PA} (mm^3/s)	Manual	1	0.34 (0.2)	0.35 (0.17)	–0.002 (0.04)	0.97 (19)
	Auto	1	0.36 (0.21)	0.36 (0.15)	0.039 (0.077)	0.63 (19)
	Auto	2	0.35 (0.2)	0.34 (0.14)	0.025 (0.043)	0.56 (17)
	Auto	3	0.34 (0.15)	0.33 (0.14)	0.004 (0.037)	0.92 (19)

Table 5
Coefficients of age from the quasi-Poisson regression (for count) and linear mixed effects model analyses and corresponding p values and number of pairs. An asterisk in the last column indicates significant difference from zero.

	Segmentation	Scan	Coefficient	P value (n)
PA Count (1/y)	Manual	1	–0.01 (0.0068)	0.14 (19)
	Auto	1	–0.011 (0.007)	0.14 (19)
	Auto	2	–0.013 (0.007)	0.072 (18)
	Auto	3	–0.012 (0.007)	0.096 (19)
PA_{perp} Count (1/y)	Manual	1	0.0014 (0.01)	0.89 (19)
	Auto	1	0.00095 (0.011)	0.93 (19)
	Auto	2	0.002 (0.01)	0.84 (18)
	Auto	3	–0.003 (0.01)	0.77 (19)
D_{PA} (mm/y)	Manual	1	0.00043 (0.00065)	0.52 (19)
	Auto	1	–0.00001 (0.0008)	0.99 (19)
	Auto	2	0.0013 (0.00073)	0.088 (17)
	Auto	3	0.00091 (0.00042)	0.034 (19)*
V_{PA} (cm/s/y)	Manual	1	–0.015 (0.0081)	0.085 (19)
	Auto	1	–0.02 (0.0081)	0.027 (19)*
	Auto	2	–0.015 (0.0097)	0.14 (17)
	Auto	3	–0.012 (0.0065)	0.09 (19)
$Q_{PA}(mm^3/s/y)$	Manual	1	0.00013 (0.002)	0.94 (19)
	Auto	1	0.00023 (0.002)	0.91 (19)
	Auto	2	0.0015 (0.0018)	0.4 (17)
	Auto	3	0.0001 (0.0014)	0.94 (19)

and R_2* did not show significant difference. The lower PA velocity might be related to increased tortuosity of PAs in the patients. Increase tortuosity in retinal areries is commonly observed in patients with DM [25] and in patients with SVD [26]. Increased PA tortuosity can reduce flow induced phase changes because the flow directions can deviate more from the direction of velocity encoding gradient in tortuous PAs leading to decrease in measured velocity [27]. Brain atrophy, which is common among patients with chronic DM [28], will result in tortuous PAs if the total lengths of PAs remain constant. The observed positive and negative coefficients of age for D_{PA} and V_{PA}, respectively, are also consistent with increased tortuosity with aging. Tortuous PA are expected to have larger size when projected onto the imaging slice, which would likely result in higher measured D_{PA}.

Reduction in cerebral blood flow has also been reported in cortical and subcortical gray matter regions in patients with DM [29–31], which may reflect a reduced metabolic demand as a result of brain atrophy. Similarly reduction might be present in the WM, which is more difficult to detect due to very low signal in the WM in arterial spin labelling MRI. Reduced blood flow can likely cause reductions in all PA parameters (count, D_{PA}, V_{PA}, and Q_{PA}). The absence in count D_{PA}, and Q_{PA} differences might be due to their large intersubject variations and measurement errors, especially for Q_{PA}.

The motion correction was found to increase the count and contrast of PAs for motion scores above 0.8 mm [22]. Although no difference in motion score was observed between DM and HC groups, slightly more scans had motion scores >0.8 mm in the DM group, suggesting a potential benefit for motion correction in reducing motion related artificial differences in PA parameters. In addition, the DM group showed higher tendancy for fast motion, as reflected by the higher residual after 5th order polynomial fit to remove slow motion in the motion parameter time courses. Fast motion cannot be corrected using the prospective motion correction because of the long time it takes to acquire navigator images (4.68 s) [22]. Faster motion correction techniques should be developed to investigate whether or not more frequent faster motion contributed to the observed difference in V_{PA}.

Our study was carried out in people with diabetes mostly before the occurrence of severe SVD manifested by lacunar infarcts or Fazekas score > 2. Studying patients with more severe manifestations of SVD could increase the effect sizes of D_{PA}, V_{PA}, and Q_{PA} differences. Longitudinal studies on the same vessels can eliminate the inter-subject variations and sampling bias, thus potentially improving the statistical power for detecting such changes. Additionaly, pulsatility changes might occur even earlier than D_{PA}, V_{PA}, and Q_{PA} changes. Although pulsatility measurement has higher uncertainty (coeffiicienty of repeatability 50% after averaging across all vessels in the slice [21]) than D_{PA}, V_{PA}, and Q_{PA} at individual vessel level, thus entailing averaging across the imaging slice [21,32], its potentially larger change in the early stage may compensate for the higher uncertainty rendering larger effect sizes for detecting early PA abnormalities.

The measured coefficient of repeatability for V_{PA} is similar to an earlier study (0.76 cm/s vs 0.73 cm/s) that used similar imaging protocol [15]. However, the coefficients of repeatability for D_{PA} and Q_{PA} are greater in the current study: 0.09 mm vs 0.052 mm for D_{PA} and 0.19 mm^3/s vs 0.12 mm^3/s for Q_{PA}. The reason of the increased varitions remains unclear but might be related to difference in SNR between the head coils (single channel vs multi-channel excitation) in the two

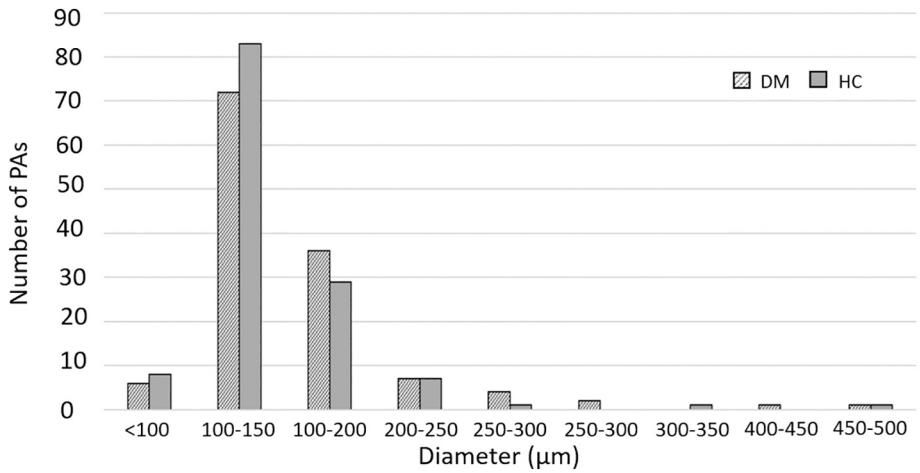

Fig. 4. Histogram showing frequencies of the diameters of penetrating arterioles in 129 vessels from 19 participants with diabetes (DM) and 130 vessels from 19 controls.

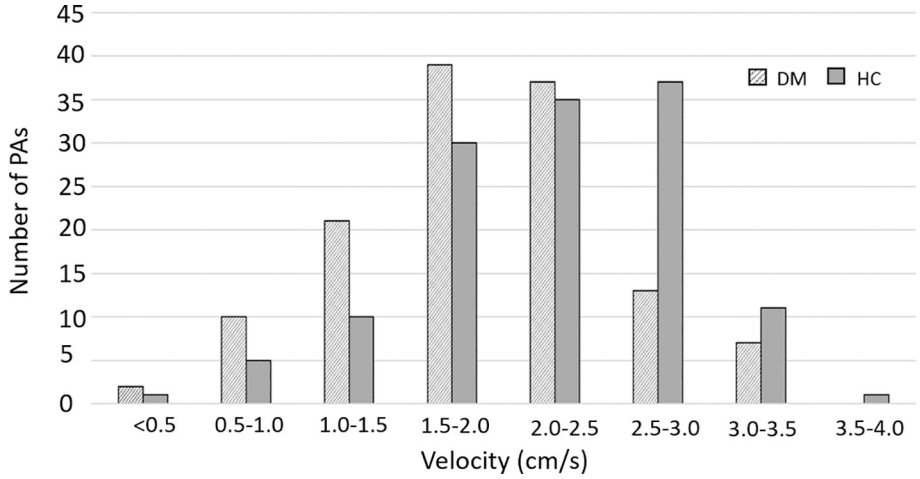

Fig. 5. Histogram showing frequencies of the velocities within penetrating arterioles in 129 vessels from 19 participants with diabetes mellitus (DM) and 130 vessels from 19 controls.

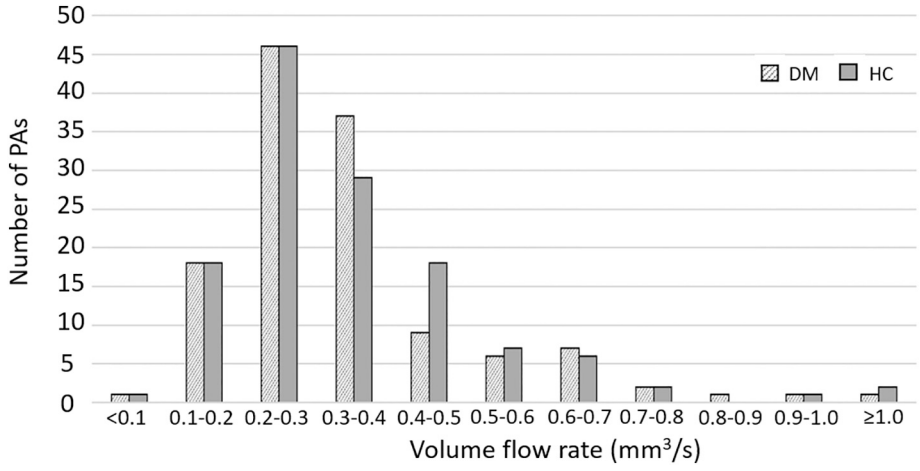

Fig. 6. Histogram showing frequencies of the volume flow rates within penetrating arterioles in 129 vessels from 19 participants with diabetes mellitus (DM) and 130 vessels from 19 controls.

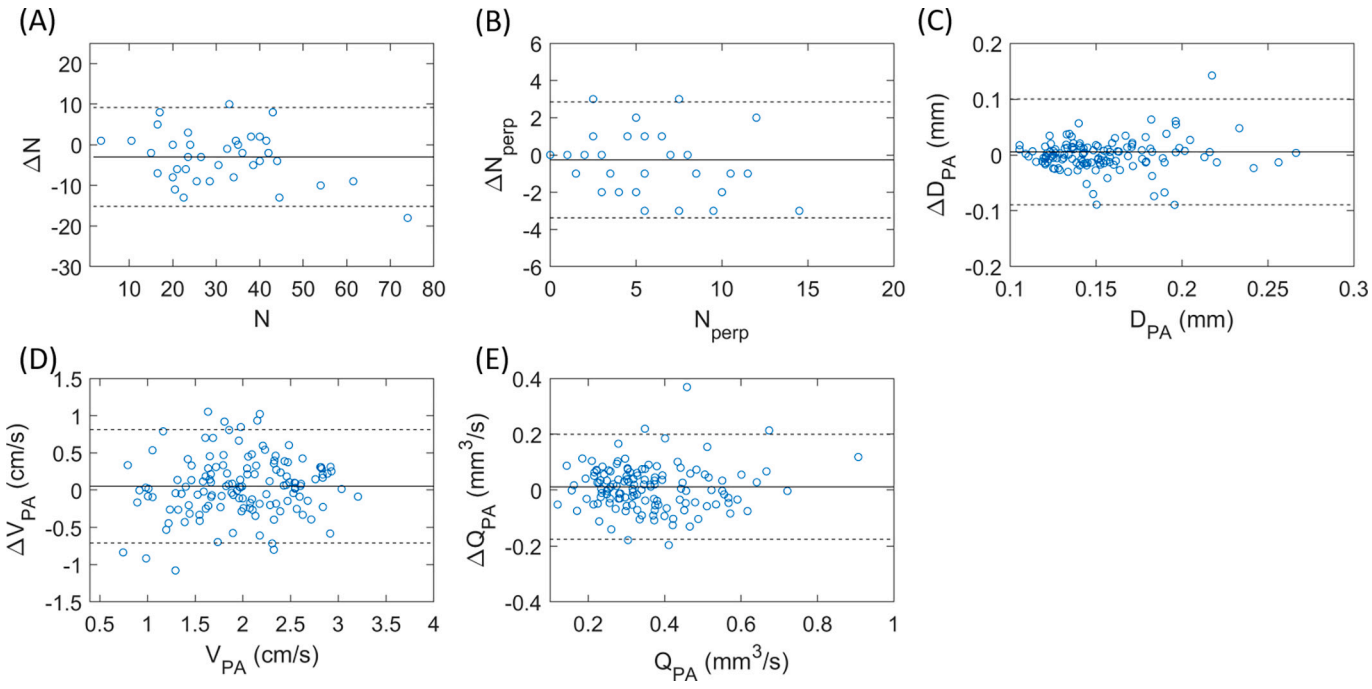

Fig. 7. Bland-Altman plots of (A) PA count, (B) PA_{perp} count, (C) D_{PA}, (D) V_{PA}, and (E) Q_{PA} of automatically segmented PAs from scans 1 and 3. In (A) and (B), each data point represents one subject, while in (C)-(E), each data point represents one PA.

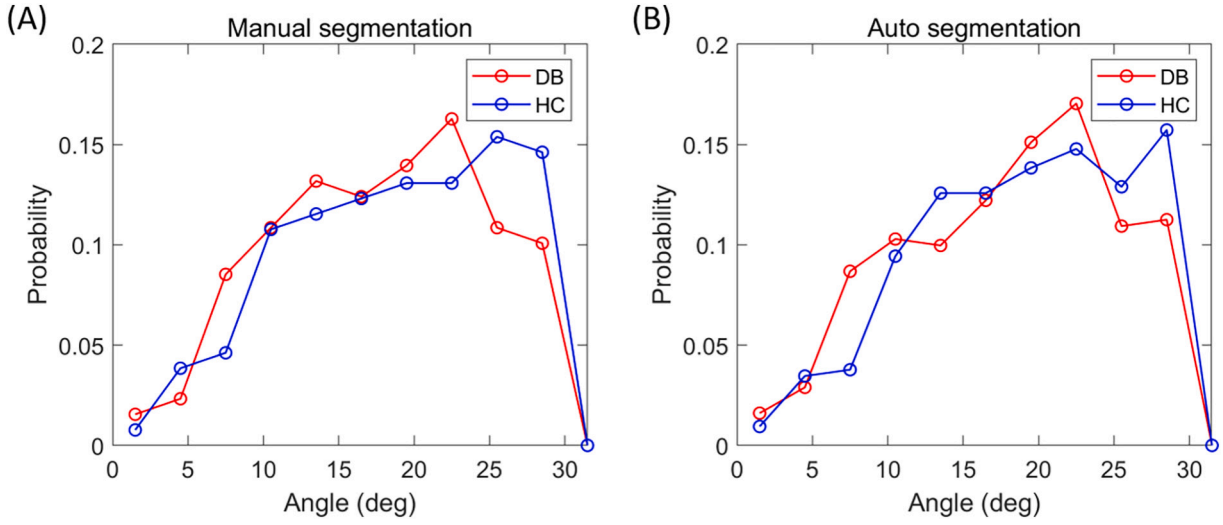

Fig. 8. Histogram of PA tilt angles from the slice normal direction for manual and automatically segmented PA clusters. Only PAs that can match a PVS and has an angle $\leq 30^{o}$ are included.

studies. On the other hand, the positive predictive value, sensitivity, and dice similarity index of the automatically segmented PA masks are consistent with values in another earlier study [22].

Our study has several limitations. Although our study focused on the effects of DM on the small vessels, we did not exclude patients who had other vascular risk factors. The DM group also had more subjects with hypertension and history of smoking. Many participants did not have lipid profiles. Thus, the contributions of the other risk factors to the observed PA difference cannot be ruled out. MBAC assumed PAs to be cylinders that are perpendicular to the imaging plane. Such assumptions are unlikely to be valid in vivo and may have led to the observed difference in V_{PA}. Due to the limited SNR, PC-MRI can only visualize PAs with diameters >78 μm, missing the very smallest [33,34]. However, the vessels with diameters >78 μm encompass the majority of those affected by SVD in the cerebral WM. Furthermore, due to the limited coverage of single slice acquisition, only a small fraction of PAs that had diameter > 78 μm could be measured and the measurement could only be made at a single position along the PA length. Difference in sampling biases between DM and controls could result in artificial differences in measured PA parameters. In the future, meaurements at multiple positions and orientations should be carried out to avoid the potential sampling biases inherent in single slice studies.

5. Conclusions

In conclusion, we have demonstrated in vivo quantitative measurements of human WM PA size and flow characteristics with ultra-high field 7 T MRI that are discriminative of disease state and age. Coupled

with techniques to examine the function of these vessels, our findings provide a basis for further studies to characterize the alterations in WM PAs that occur in patients with cardiovascular risks factors such as diabetes and hypertension and their role in producing the overt clinical and imaging manifestations of SVD [35–37].

Funding source

The work was supported by the National Center for Advancing Translational Sciences (NCATS), National Institutes of Health, through Grant Award Number UL1TR002489.

Author contributions

Concept and design: XZ, WJP.
Data acquisition and analysis: XZ, JJ, TL, WJP.
Drafting of the manuscript: XZ, WJP.

Declaration of Competing Interest

None.

Data availability

All MRI, demographic, and clinical data analyzed in this study can be downloaded from https://data.mendeley.com/datasets/89f6x2fnks/1. The code for MBAC analysis can be downloaded from https://data.mendeley.com/datasets/8bsgw4rhtr/3 published in an earlier study.

Acknowledgements

We thank Dr. John Buse at the Department of Endocrinology, the University of North Carolina at Chapel Hill for suggestions, and Dr. Andrea Bozoki at the Department of Neurology, University of North Carolina at Chapel Hill for recommending the MoCA test.

Appendix A. Supplementary data

Supplementary data to this article can be found online at https://doi.org/10.1016/j.mri.2023.03.015.

References

[1] Grinberg LT, Thal DR. Vascular pathology in the aged human brain. Acta Neuropathol 2010;119(3):277–90.
[2] Lammie GA. Hypertensive cerebral small vessel disease and stroke. Brain Pathol 2002;12(3):358–70.
[3] Lammie GA, Brannan F, Slattery J, Warlow C. Nonhypertensive cerebral small-vessel disease. An autopsy study. Stroke 1997;28(11):2222–9.
[4] White H, Boden-Albala B, Wang C, Elkind MS, Rundek T, Wright CB, et al. Ischemic stroke subtype incidence among whites, blacks, and Hispanics: the northern Manhattan study. Circulation 2005;111(10):1327–31.
[5] Bokura H, Kobayashi S, Yamaguchi S, Iijima K, Nagai A, Toyoda G, et al. Silent brain infarction and subcortical white matter lesions increase the risk of stroke and mortality: a prospective cohort study. J Stroke Cerebrovasc Dis 2006;15(2):57–63.
[6] Longstreth Jr WT, Manolio TA, Arnold A, Burke GL, Bryan N, Jungreis CA, et al. Clinical correlates of white matter findings on cranial magnetic resonance imaging of 3301 elderly people. The Cardiovasc Health Study Stroke 1996;27(8):1274–82.
[7] Vermeer SE, Hollander M, van Dijk EJ, Hofman A, Koudstaal PJ, Breteler MM, et al. Silent brain infarcts and white matter lesions increase stroke risk in the general population: the Rotterdam scan study. Stroke 2003;34(5):1126–9.
[8] van der Flier WM, van Straaten EC, Barkhof F, Verdelho A, Madureira S, Pantoni L, et al. Small vessel disease and general cognitive function in nondisabled elderly: the LADIS study. Stroke 2005;36(10):2116–20.
[9] Herrmann LL, Le Masurier M, Ebmeier KP. White matter hyperintensities in late life depression: a systematic review. J Neurol Neurosurg Psychiatry 2008;79(6):619–24.
[10] de Laat KF, van Norden AG, Gons RA, van Uden IW, Zwiers MP, Bloem BR, et al. Cerebral white matter lesions and lacunar infarcts contribute to the presence of mild parkinsonian signs. Stroke 2012;43(10):2574–9.
[11] de Laat KF, Tuladhar AM, van Norden AG, Norris DG, Zwiers MP, de Leeuw FE. Loss of white matter integrity is associated with gait disorders in cerebral small vessel disease. Brain 2011;134(Pt 1):73–83.
[12] Wardlaw JM, Smith EE, Biessels GJ, Cordonnier C, Fazekas F, Frayne R, et al. Neuroimaging standards for research into small vessel disease and its contribution to ageing and neurodegeneration. The Lancet Neurol 2013;12(8):822–38.
[13] Wardlaw JM, Dennis MS, Warlow CP, Sandercock PA. Imaging appearance of the symptomatic perforating artery in patients with lacunar infarction: occlusion or other vascular pathology? Ann Neurol 2001;50(2):208–15.
[14] Fisher CM. The arterial lesions underlying lacunes. Acta Neuropathol 1968;12(1):1–15.
[15] Zong X, Lin W. Quantitative phase contrast MRI of penetrating arteries in centrum semiovale at 7T. NeuroImage 2019;195:463–74.
[16] Schnerr RS, Jansen JFA, Uludag K, Hofman PAM, Wildberger JE, van Oostenbrugge RJ, et al. Pulsatility of Lenticulostriate arteries assessed by 7 tesla flow MRI-measurement, reproducibility, and applicability to aging effect. Front Physiol 2017;8:961.
[17] Perosa V, Arts T, Assmann A, Mattern H, Speck O, Oltmer J, et al. Pulsatility index in the basal ganglia arteries increases with age in elderly with and without cerebral small vessel disease. AJNR Am J Neuroradiol 2022;43(4):540–6.
[18] Arts T, Onkenhout LP, Amier RP, van der Geest R, van Harten T, Kappelle J, et al. Non-invasive assessment of damping of blood flow velocity Pulsatility in cerebral arteries with MRI. J Magn Reson Imaging 2022;55(6):1785–94.
[19] Geurts LJ, Zwanenburg JJM, Klijn CJM, Luijten PR, Biessels GJ. Higher Pulsatility in cerebral perforating arteries in patients with small vessel disease related stroke, a 7T MRI study. Stroke 2018;50(1). STROKEAHA118022516-STROKEAHA.
[20] Nasreddine ZS. MoCA test: validation of a five-minute telephone version. Alzheimers Dement 2021;17(S8):e057817.
[21] Bouvy WH, Geurts LJ, Kuijf HJ, Luijten PR, Kappelle LJ, Biessels GJ, et al. Assessment of blood flow velocity and pulsatility in cerebral perforating arteries with 7-T quantitative flow MRI. NMR Biomed 2016;29(9):1295–304.
[22] Moore J, Jimenez J, Lin W, Powers W, Zong X. Prospective motion correction and automatic segmentation of penetrating arteries in phase contrast. MRI at 7 T. Magn Reson Med 2022;88(5):2088–100.
[23] Lian C, Zhang J, Liu M, Zong X, Hung SC, Lin W, et al. Multi-channel multi-scale fully convolutional network for 3D perivascular spaces segmentation in 7T MR images. Med Image Anal 2018;46:106–17.
[24] Fazekas F, Kleinert R, Offenbacher H, Schmidt R, Kleinert G, Payer F, et al. Pathologic correlates of incidental MRI white matter signal hyperintensities. Neurology 1993;43(9):1683–9.
[25] Song Y, Zhou Z, Liu H, Du R, Zhou Y, Zhu S, et al. Tortuosity of branch retinal artery is more associated with the genesis and progress of diabetic retinopathy. Front Endocrinol (Lausanne) 2022;13:972339.
[26] Biffi E, Turple Z, Chung J, Biffi A. Retinal biomarkers of cerebral small vessel disease: a systematic review. PLoS One 2022;17(4):e0266974.
[27] Brown WR, Moody DM, Challa VR, Thore CR, Anstrom JA. Venous collagenosis and arteriolar tortuosity in leukoaraiosis. J Neurol Sci 2002;203-204:159–63.
[28] Brundel M, Kappelle LJ, Biessels GJ. Brain imaging in type 2 diabetes. Eur Neuropsychopharmacol 2014;24(12):1967–81.
[29] Bangen KJ, Werhane ML, Weigand AJ, Edmonds EC, Delano-Wood L, Thomas KR, et al. Reduced regional cerebral blood flow relates to poorer cognition in older adults with type 2 diabetes. Front Aging Neurosci 2018;10:270.
[30] Cui Y, Liang X, Gu H, Hu Y, Zhao Z, Yang XY, et al. Cerebral perfusion alterations in type 2 diabetes and its relation to insulin resistance and cognitive dysfunction. Brain Imaging Behav 2017;11(5):1248–57.
[31] Jansen JF, van Bussel FC, van de Haar HJ, van Osch MJ, Hofman PA, van Boxtel MP, et al. Cerebral blood flow, blood supply, and cognition in type 2 diabetes mellitus. Sci Rep 2016;6(1):10.
[32] Geurts L, Biessels GJ, Luijten P, Zwanenburg J. Better and faster velocity pulsatility assessment in cerebral white matter perforating arteries with 7T quantitative flow MRI through improved slice profile, acquisition scheme, and postprocessing. Magn Reson Med 2018;79(3):1473–82.
[33] Zhu G-m, Zhang W-w, Liu Y, Li J. Arterioles in cerebral amyloid angiopathy and vascular dementia. Chin Med J 2009;122(24):2985–8.
[34] Huang YH, Zhang WW, Lin L, Feng J, Zhao XX, Guo WH, et al. Could changes in arterioles impede the perivascular drainage of interstitial fluid from the cerebral white matter in leukoaraiosis? Neuropathol Appl Neurobiol 2010;36(3):237–47.
[35] Powers W, An H, Oakes J, Eron J, Robertson K, Sen S. Autoregulation of White matter cerebral blood flow to arterial pressure changes in Normal subjects. J Neurol Disord Stroke 2021;8(3).
[36] Blair GW, Thrippleton MJ, Shi Y, Hamilton I, Stringer M, Chappell F, et al. Intracranial hemodynamic relationships in patients with cerebral small vessel disease. Neurology 2020;94(21). e2258-e69.
[37] Thrippleton MJ, Shi Y, Blair G, Hamilton I, Waiter G, Schwarzbauer C, et al. Cerebrovascular reactivity measurement in cerebral small vessel disease: rationale and reproducibility of a protocol for MRI acquisition and image processing. Int J Stroke 2018;13(2):195–206.